



**HAL**  
open science

## Experimental characterization of rigid-scatterer hyperuniform distributions for audible acoustics

Elie Chéron, Jean-Philippe Groby, Vincent Pagneux, Simon Félix, Vicent Romero-García

► **To cite this version:**

Elie Chéron, Jean-Philippe Groby, Vincent Pagneux, Simon Félix, Vicent Romero-García. Experimental characterization of rigid-scatterer hyperuniform distributions for audible acoustics. *Physical Review B*, 2022, 106 (6), pp.064206. 10.1103/PhysRevB.106.064206 . hal-03862881


**HAL Id: hal-03862881**

**<https://univ-lemans.hal.science/hal-03862881v1>**

Submitted on 4 Oct 2024

**HAL** is a multi-disciplinary open access archive for the deposit and dissemination of scientific research documents, whether they are published or not. The documents may come from teaching and research institutions in France or abroad, or from public or private research centers.

L'archive ouverte pluridisciplinaire **HAL**, est destinée au dépôt et à la diffusion de documents scientifiques de niveau recherche, publiés ou non, émanant des établissements d'enseignement et de recherche français ou étrangers, des laboratoires publics ou privés.

**Experimental characterization of rigid-scatterer hyperuniform distributions for audible acoustics**Elie Chéron,<sup>1</sup> Jean-Philippe Groby<sup>1</sup>, Vincent Pagneux<sup>1</sup>, Simon Félix<sup>1</sup> and Vicent Romero-García<sup>1,2,\*</sup><sup>1</sup>Laboratoire d'Acoustique de l'Université du Mans (LAUM), UMR 6613, Institut d'Acoustique - Graduate School (IA-GS), CNRS, Le Mans Université, France<sup>2</sup>Instituto Universitario de Matemática Pura y Aplicada (IUMPA), Departamento de Matemática Aplicada, Universitat Politècnica de València, Camino de Vera s/n, 46022, València, Spain (Received 9 December 2021; revised 26 July 2022; accepted 28 July 2022; published 16 August 2022)

The wave transport properties of two-dimensional stealthy hyperuniform distributions of rigid scatterers embedded in a waveguide are experimentally characterized for scalar waves in airborne audible acoustics. The nonresonant nature of the scatterers allows us to directly link these properties to the geometric distribution of points through the structure factor. The transport properties are analyzed as a function of the stealthiness  $\chi$  of their hyperuniform point pattern and compared to those of a disordered material in the diffusive regime, which are characterized by the Ohm's law through both the classical mean free path and the corrected mean free path by the collective approximation considering the effects of correlation. Different scattering regimes are theoretically and numerically identified showing transparent regions, isotropic band gaps, and anisotropic scattering depending on  $\chi$ . The robustness of these scattering regimes to losses, which are unavoidable in audible acoustics is experimentally unveiled.

DOI: [10.1103/PhysRevB.106.064206](https://doi.org/10.1103/PhysRevB.106.064206)**I. INTRODUCTION**

Wave transport properties in complex systems are one of the most studied topics in wave physics. Waves traveling in these complex systems often undergo multiple scattering. Depending on both the distribution of scatterers and the physical properties of each scatterer, several phenomena can appear in different ranges of frequencies such as Anderson localization [1,2] in disordered systems or wave collimation [3] and focusing [4] in periodic systems. The opening of band gaps is probably the most celebrated phenomenon in periodic media and has given rise to a plethora of studies in electromagnetic [5] or elastic [6] wave transport. In photonic [7,8] or phononic [9,10] crystals, two main phenomena contribute to the generation of the band gaps [11,12]: The Bragg scattering (based on geometrical arguments) and the excitation of the single scatterer Mie resonances (based on intrinsic local properties of the scatterer) [13,14]. While Bragg scattering establishes the necessary condition for the opening of band gaps, Mie resonances are helpful for the opening of full band gaps in two or three dimensional systems [12,15,16].

Recently, stealthy hyperuniform materials have emerged as amorphous systems presenting unique wave transport properties due to the correlated disorder and therefore have opened new venues for controlling waves [17–23]. Hyperuniform materials are based on the concept of hyperuniformity, i.e., the suppression of the long-range density fluctuations of the point pattern [24–29]. Stealthy hyperuniform point patterns are characterized by the stealthiness  $\chi$ , which imposes constraints on the structure factor in the reciprocal space. Several papers

have shown the evolution of the point distribution with  $\chi$  in 1D [23,27,30], 2D [25–27], and 3D [26,27] systems. Three classes of point patterns can be distinguished in function of  $\chi$ : Disordered, wavy-crystalline, and crystalline [26]. For values of  $\chi \lesssim 0.45$ , isotropic structure factors in the reciprocal space are obtained, i.e., with low angular fluctuations corresponding to disordered systems. Anisotropic structure factors in the reciprocal space are obtained corresponding to wavy-crystalline and crystalline point patterns for values  $\chi \gtrsim 0.55$ .

Wave transport properties in materials made of hyperuniform distributions of scatterers, have recently been analyzed for electromagnetic [17,18,31] and elastic [20,32] waves by combining the geometric properties of stealthy hyperuniform point patterns with the Mie resonances of the scatterers. So designed hyperuniform materials are transparent to incident long-wavelength excitation and present isotropic band gap at shorter wavelengths with  $\chi \lesssim 0.45$ . This last feature is in opposition to the quasiperiodic systems in which anisotropic band gaps are created with  $\chi \gtrsim 0.5$  [29,33]. Waveguides with arbitrary paths have been designed by exploiting these isotropic full band gaps [17,18]. Nevertheless, Mie resonances are always used in all these examples, although hyperuniform materials should be uniquely characterized by the spatial Fourier transform of the point pattern. In this sense, the use of nonresonant scatterers seems the best option to discriminate between scattering produced by the local resonances and the scattering produced by the peaks of the structure factor due to the point pattern distribution. For example, when disorder is introduced into periodic systems, Bragg and Mie resonances together have been shown to play important roles [11,15]: The band gap closes rapidly as disorder increases when the gap is due to Bragg scattering, while it is more robust, when it is due to Mie resonances [12,16]. Recently, several papers

\*virogar1@mat.upv.es

have analyzed the interplay of these two phenomena in hyperuniform materials [22,23]. It has been shown that when the local resonances are tuned in the transparent frequency band of the hyperuniform material, a dip of transmission is produced [22], while if the resonance is close to the Bragg frequency, the isotropic band gaps in hyperuniform materials are wider [23]. The acoustic system presented in this paper allows to use nonresonant scatterers to build the hyperuniform materials and therefore ensures that the transport properties are only due to hyperuniform point pattern distribution used to build the material.

In this paper, the wave transport properties of two-dimensional (2D) hyperuniform distributions of rigid scatterers embedded in a rectangular cross-sectional waveguide are numerically and experimentally characterized for scalar waves in airborne audible acoustics. In this regime, solid scatterers are usually nonpenetrable (impervious) and present a Neumann boundary condition due to the huge impedance mismatch between their properties and those of the air (host medium) [34]. These scatterers are thus considered acoustically rigid and do not resonate. Therefore, airborne audible acoustics seems to be a good candidate to investigate the connection between the wave transport properties of a given distribution of rigid scatterers and its corresponding structure factor. We perform both a multimodal method (Sec. III B 1) and a full wave solution of the Helmholtz equation (finite element method, Sec. III B 2) to obtain the transport properties of the system made of a discrete distribution of rigid scatterers. The obtained results with these two methods can be compared with experiments (Sec. III B 2), and with the theoretical transport properties obtained from the Ohm's law using the mean free path of the media calculated with and without the effects of correlation (Sec. III B 3). In order to consider the effect of correlation, we make use of the collective approximation [35]. Moreover, viscothermal losses are not avoidable in acoustics. As a consequence, we solve the problem considering an absorption length in order to account for the viscothermal losses. We pay attention to the transition from a random to a periodic distribution of scatterers in hyperuniform materials by changing the stealthiness of the system  $\chi$ . The transport properties for low values of  $\chi$  (uncorrelated disorder) are well captured by the Ohm's law using the classical mean free path of the media. As soon as the value of  $\chi$  increases, the transmission calculated with the Ohm's law by means of the corrected mean free path by the collective approximation [35] evidences the presence of the isotropic band gaps, which becomes anisotropic for  $\chi \gtrsim 0.5$ . These results emphasize the relation of the transport properties in hyperuniform materials with the distribution of points through the structure factor by eliminating the local resonance of the scatterers. The good agreement between simulations, experiments, and theory shows that the transport properties of the hyperuniform materials are robust to the presence of losses.

## II. HYPERUNIFORM POINT PATTERNS

Let us consider a distribution of  $N$  points located at positions  $\mathbf{r}_i$  ( $i = 1, \dots, N$ ) inside a square domain of side  $L$ , as shown in Fig. 1(a). The structure factor  $S(\mathbf{q})$  of the point

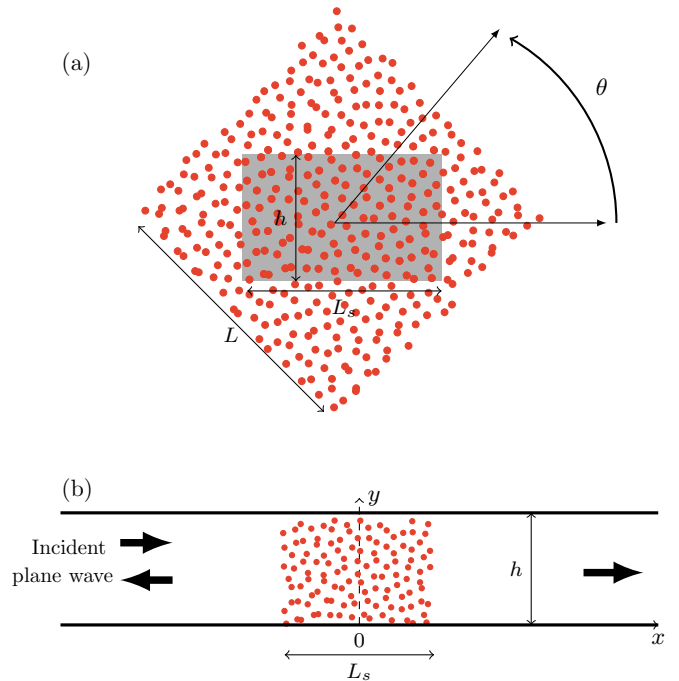


FIG. 1. (a) Hyperuniform point pattern of  $N = 600$  points in a square region of side  $L$ . The point pattern can be rotated an angle  $\theta$  with respect to its center. The point pattern has been generated by using the procedure described in the main text and in Refs. [29,36,37]. The point pattern shown in the area  $L_s \times h$  delimited by the dashed lines is used to extract the point pattern that will be used to make a hyperuniform material by placing rigid scatterers at those positions. Inside this area the number of points will be  $N_s \simeq 200$ . We characterize the acoustic wave transport properties of such material by measuring the scattering coefficients of the sample when embedded in a rectangular acoustic waveguide. (b) Shows a picture of the acoustic waveguide used in the experimental set-up displaying how the material is placed inside. The material is excited by an incident plane wave. For each angle  $\theta$ , a different material can be created and then analyzed through the transmission coefficient as a function of the angle  $\theta$ .

pattern  $\mathbf{r}_i$  ( $i = 1, \dots, N$ ) is defined as its spatial Fourier transform and reads as follows [38,39]:

$$S(\mathbf{q}) = \frac{1}{N} \sum_{i=1}^N \sum_{j=1}^N e^{-i\mathbf{q} \cdot (\mathbf{r}_j - \mathbf{r}_i)}, \quad (1)$$

where  $\mathbf{q}$  is a vector in the Fourier space. It is worth noting here that if the point pattern is periodic, the structure factor will present the characteristic Bragg peaks [29]. For example, they are located at  $\mathbf{q}_B = (n2\pi\sqrt{N}/L, m2\pi\sqrt{N}/L)$ , with  $m, n \in \mathbb{Z}$  for a two-dimensional square array, which periodicity is  $a = L/\sqrt{N}$ . For periodic structures,  $\mathbf{q}_B$  represents the well-known vectors of the reciprocal lattice in the reciprocal space.

The hyperuniformity concept can be defined by either the local number variance  $\sigma^2(R)$  (i.e., the variance in the number of points within a randomly-thrown spherical window of radius  $R$ ) of the point pattern in the real space or by the structure factor  $S(\mathbf{q})$  in the reciprocal or Fourier space [29]. Here, we use the structure factor  $S(\mathbf{q})$ . Hyperuniform point patterns are characterized by a structure factor that vanishes

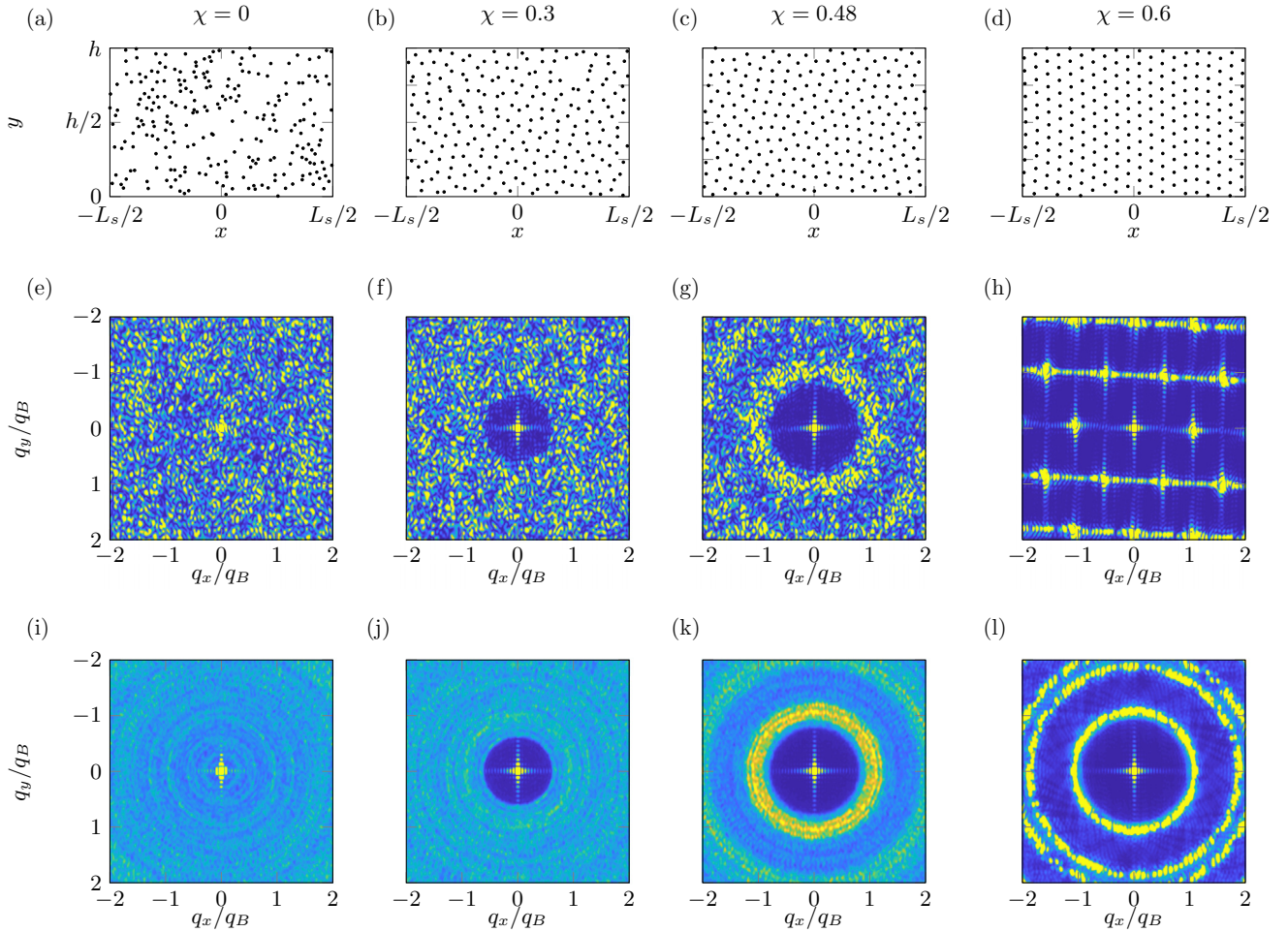


FIG. 2. [(a)–(d)] Typical configurations of two-dimensional stealthy hyperuniform points pattern scatterers placed in a wave-guide of width  $h = 400$  mm and length  $L_s = 1.5h$  for different values of  $\chi$ . Their corresponding structure factor are presented [(e)–(h)] for a single point pattern generation at initial angle  $\theta = 0$ ; [(i)–(l)] show the corresponding angularly averaged structure factor.

in the long-wavelength limit, i.e.,  $S(q \rightarrow 0) = 0$  where  $q = |\mathbf{q}|$ , while stealthy hyperuniform point patterns are characterized by a structure factor that vanishes around the origin of wavevectors,  $S(q < q_c) = 0$  with  $\mathbf{q}_c$  the cut-off reciprocal vector defining  $\Omega$  that refers to the set of the constrained reciprocal vectors ( $q < q_c$ ) [25]. The distribution of points that meets these conditions on the structure factor can be characterized by the stealthiness  $\chi$ . The stealthiness is the ratio of the number  $M(\Omega)$  of constrained reciprocal lattice vectors to the number of degrees of freedom in the real space  $d(N - 1)$  in  $d$  dimensions (if the system translational degrees of freedom are neglected) [27]. In this paper, we consider a two-dimensional system  $d = 2$  and thus  $\Omega$  is a circular region of radius  $q_c$  in the reciprocal space centered in the origin of coordinates. Considering the symmetry of the structure factor,  $S(\mathbf{q}) = S(-\mathbf{q})$ , and  $M(\Omega) = \frac{1}{2}\pi(q_c L/2\pi)^2$ , the stealthiness becomes

$$\chi = \frac{(q_c L)^2}{16\pi(N - 1)}. \quad (2)$$

It is worth noting here that the expression of  $\chi$  strongly depends on the shape of the domain  $\Omega$ . Other expressions can

be obtained when the  $\Omega$  is a square centered in the origin of coordinate with side  $q_c$  as shown in Ref. [19] for instance.

A stealthy hyperuniform point pattern characterized by a stealthiness  $\chi$  is designed with  $N = 600$  points embedded in a square area of side  $L$ . This point pattern is generated using the procedure given by the works of Zhang *et al.* [36,37] and Froufe-Pérez *et al.* [29]. For convenience and because of experimental constrains, we consider a subset of  $N_s$  points embedded in a rectangular area of size  $L_s \times h$  as shown in Fig. 1(a). Note that other stealthy hyperuniform point patterns with the same  $\chi$  can be generated by rotating the initial point pattern by an angle  $\theta$  and keeping the points located in the area  $L_s \times h$  as shown in Fig. 1(a). Our approach here is to average over a finite number of samples that are originated from a single large configuration and cropping it. This approach allows us to extract different patches with the same hyperuniformity properties [33,40].

Figures 2(a)–2(d) represents four stealthy hyperuniform point patterns made of  $N_s \simeq 200$  points, created with the previous procedure, for four different stealthiness  $\chi = [0, 0.3, 0.48, 0.6]$ . We have analyzed the evolution of the point patterns by increasing the radius of the constrained area  $q_c$ , or equivalently, by increasing the stealthiness  $\chi$ . The values



of the stealthiness are bounded between  $\chi_{\min} = 0$  and  $\chi_{\max} = \pi/4$  (when  $q_c = 2\pi\sqrt{N}/L$ ), leading respectively to Poisson's distributions and perfect crystal lattices [27]. The point pattern clearly crystallizes when the stealthiness increases and approaches to 0.5. Figures 2(e)–2(h) show the structure factor calculated by using Eq. (1) showing the corresponding point patterns due to the discretization for each point pattern. The vectors in the reciprocal space are normalized by the amplitude of the smallest Bragg reciprocal vector  $q_B = 2\pi\sqrt{N}/L$ . The circumference of the constrained area in the reciprocal space of radius  $q_c = 4\sqrt{\chi N\pi}/L$  is clearly visible. In addition, the structure factor clearly exhibits an extra isotropic region close to  $q_c$  for  $\chi = 0.48$ , where an increase of the structure factor is visible (yellow region). When  $\chi \gtrsim 0.5$ , the structure factor is anisotropic. The system behaves as a wavy-crystalline system for  $\chi = 0.6$  as described in Ref. [25]. Finally, Figs. 2(i)–2(l) show the angularly average structure factor over 60 realizations. The information on the isotropy is lost, but the cutoff wavevector of the hyperuniform materials is clearly visible, where  $S(q) = 0$  for all  $q < q_c$ . The diffraction pattern visible around  $q = 0$  is a phenomenon that appears when the Fourier Transform is calculated with a finite window. Considering rectangular windows, the diffraction pattern can be observed as soon as the sampling of the media in the real space does not correspond to the nodes of the diffraction pattern in the reciprocal space. Here, our sampling is driven by the size of the scatterers that renders the diffraction pattern by the Fourier transform visible. It can be removed by following the procedure shown in Ref. [19]. However, we prefer to keep it as it can be associated to the finite size effects of the sample and also for the sake of simplicity.

### III. ACOUSTIC WAVE TRANSPORT IN 2D HYPERUNIFORM DISTRIBUTION OF RIGID SCATTERERS

#### A. 2D Hyperuniform acoustic materials

The hyperuniform material used in this work is made by placing aluminum cylinders of radius  $r_s = 0.5$  cm at the positions of the extracted point pattern in the rectangular area of size  $L_x = 0.6$  m and  $h = 0.4$  m as schematically shown in Fig. 1(b). Figure 3(a) shows a picture of one of the 2D hyperuniform acoustic materials experimentally analyzed in this paper.

In order to acoustically characterize the 2D hyperuniform materials, they are embedded in an air filled rectangular waveguide with  $h = 0.4$  m and height  $h_z = 1.5$  cm. The cutoff frequency for the second propagating mode along the waveguide height, i.e., the  $z$  direction, is around 11 500 Hz. The studied frequency range goes from 400 Hz to 8000 Hz, in such a way that the waveguide can be considered as 2D because a single mode can exist along the  $z$  direction. The right end of the waveguide is anechoic. The system is excited by a plane wave traveling from the left to the right.

#### B. Wave transport in complex media embedded in a waveguide

The wave transport properties of such materials are obtained via their scattering coefficients, i.e., by the reflection

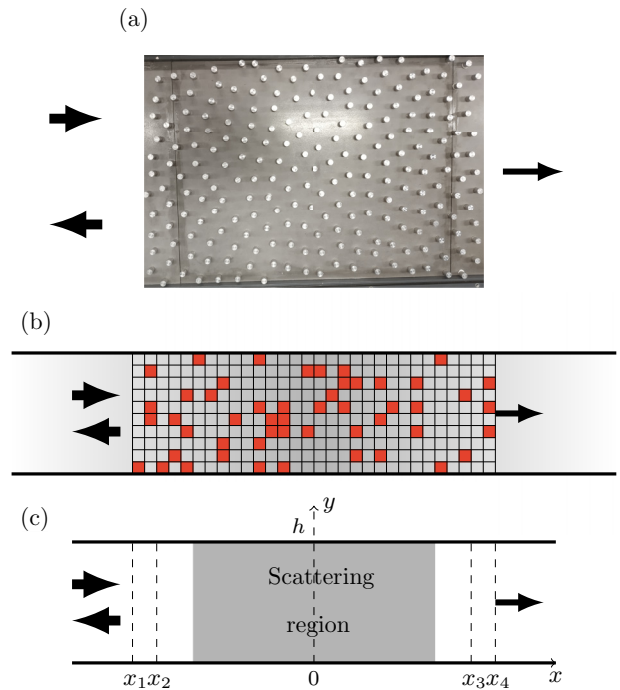


FIG. 3. (a) Top view of the experimental setup. The scattering region is made of 200 aluminum cylinder of 1-cm diameter. (b) Schematics representation of the scattering problem for numerical computation. (c) Schematics representation of the scattering problem with the four lines at  $x_1, x_2, x_3,$  and  $x_4$  used to measure pressure field.

and transmission coefficients defined in this section. The wave transport properties of the hyperuniform materials can thus be theoretically, numerically, and experimentally characterized as explained here. This allows us to analyze the relation between the properties of the point pattern in the reciprocal space with the scattering of the system.

#### 1. Multimodal method

The wave transport properties of the stealthy hyperuniform materials are obtained numerically by a multimodal method where the Helmholtz equation ( $\nabla^2 p + k^2 p = 0$  with  $\partial_n p = 0$  on the rigid boundaries) is projected on the local transverse modes and then solved using an admittance matrix as described in Refs. [41–45]. This procedure is detailed in the Supplemental Material [46]. To solve this problem, we discretize the scattering region on a regular grid of size  $\Delta_x = \Delta_y$ . The scattering medium of length  $L = N_x \Delta_x$  is thus constituted of  $N_x$  columns numbered as  $i = \{0, 1, \dots, i, \dots, N_x\}$  and  $N_y$  rows numbered as  $j = \{0, 1, \dots, j, \dots, N_y\}$ . Thus,  $h = N_y \Delta_y$  [see Fig. 3(b)]. Here, each column is assumed invariant along the  $x$  axis and the associated scattering matrix of the  $i$ th column  $S_i$  is solved using the admittance matrix. The global scattering matrix  $S$  of the system is calculated by assembling the single scattering matrix of each column characterizing the scattering in the far field region, so accounting for the propagative components. The global scattering matrix reads

$$S = \begin{pmatrix} R^+ & T^- \\ T^+ & R^- \end{pmatrix}, \quad (3)$$

where  $\mathbf{R}^+$ ,  $\mathbf{R}^-$  are the reflection coefficients matrix from each side of the full scattering medium and  $\mathbf{T}^+$  and  $\mathbf{T}^-$  the corresponding transmission matrices. We notice that the system is reciprocal, i.e.,  $\mathbf{S}^T = \mathbf{S}$  ( $T$  meaning transpose) [47].

The general solution for the acoustic pressure  $\psi(x, y)$  can be expressed considering the separation of variables as follows:

$$\psi(x, y) = \sum_m p_m(x) h_m(y), \quad (4)$$

where  $h_m(y)$ ,  $m \in \mathbb{N}$ , is the complete set of orthonormal functions, solutions of the eigenproblem  $h_m''(y) = -k_y^2 h_m(y)$  (with  $h_m' \equiv dh_m/dy$ ) considering rigid boundary conditions at  $y = 0$  and  $y = h$ , i.e.,  $h_m'(h) = h_m'(0) = 0$ . The transmission of an incident mode  $n$  to a transmitted mode  $m$  is given by

$$p_m^+(L/2) = \sum_n T_{mn} p_n^+(-L/2), \quad (5)$$

where  $T_{mn}$  are the components of the transmission matrix. The conductance of the system can be calculated directly from these coefficients using the Landauer formula [48]

$$g = \text{Tr}(\mathbf{T}\mathbf{T}^\dagger), \quad (6)$$

with  $\text{Tr}()$  the trace and  $\mathbf{T}^\dagger$ , the adjoint of  $\mathbf{T}$ . In this paper, the average conductance over all angles  $\theta \in [0; 2\pi]$  is denoted  $\langle g \rangle$ .

We assume that the wave energy is distributed over all modes via a multiple scattering process. The sum of the transmission coefficients, corresponding to the transmission of the incident plane wave, is linked to the conductance by

$$\langle T \rangle = \langle g \rangle / N_{\text{mod}}, \quad (7)$$

where  $N_{\text{mod}}$  is the number of propagating modes considered in the solution.

## 2. Experimental and numerical full wave characterization of the scattering properties

In addition to the multimodal calculations described above, we reconstruct the scattering parameters of the material located in the scattering region as shown in Fig. 3(c). We both experimentally measure and numerically evaluate the pressure field along the  $y$  axis of the waveguide at 41 equidistant positions. Four lines separated by a distance of  $x_2 - x_1 = x_4 - x_3 = 1.5$  cm upstream ( $x_1, x_2$ ) and downstream ( $x_3, x_4$ ) are considered to separate both right-going and left-going waves on both sides of the sample. On the left-hand side ( $x < -L_s/2$ ), modes are associated to complex pressures,  $p_n^\pm(x) = c_n^\pm e^{\pm ik_n x}$ , while on the right-hand side [ $x > L_s/2$ , assuming anechoic termination, i.e.,  $p_n^-(x) = 0$ ], modes are only associated to complex pressures  $p_n^+(x) = d_n^+ e^{ik_n x}$ . We note that in this paper the time harmonic convention is  $e^{-i\omega t}$ .

The complex coefficients  $c_n^\pm$  and  $d_n^+$  can be obtained via the following approximation of the integral projection on modes  $h_n$ :

$$p_n^+(x) + p_n^-(x) \simeq \sum_i \psi(x, y_i) h_n(y_i), \quad (8)$$

where  $\psi(x, y_i)$  is the evaluated/measured pressure at the  $i$ th position along the  $y$  direction of the waveguide at position  $x$ .

The transmission, through the sample, of an incident plane wave  $n = 0$  to the  $m$ th mode is given by the transmission coefficient

$$p_m^+(L/2) = T_{m0} p_0^+(-L/2). \quad (9)$$

The numerical simulations have been conducted with the acoustic module of COMSOL Multiphysics, considering perfectly matched layers (PML) at the anechoic termination of the waveguide. In the experimental set-up, the anechoic termination is made of a foam block of triangular shape. In the experiments, the plane wave is generated by a set of nine equally-spaced identical high-speakers mounted on the left-end side of the waveguide providing a quasi plane wave excitation along the frequency range of the study.

## 3. Wave transport properties of a disordered material

The wave transport properties of a disordered material made of a random spatial distribution of scatterers embedded in a waveguide can be described with a single scale parameter  $s = L_s/\ell_s$  [49,50]. The scattering mean free path  $\ell_s$  measures the average distance needed for the wave to undergo enough scattering to lose the information of its initial incident direction. The scattering mean free path can be calculated from the number density of scatterers  $\sigma_n$  and the scattering cross section of a single scatterer  $\sigma_s$ . However, this cannot be generally computed in correlated disordered systems. The so-called collective approximation [35] should be used instead, since this approximation explicitly includes the structure factor of the correlated structure. The structural correlations can be seen as a modification of the angular scattering pattern of the individual scatterers and be accounted for by correcting the expression of the single scatterer differential scattering cross section  $d\sigma/d\theta$  by the static structure factor  $S(\mathbf{q})$  as  $\frac{d\sigma_s^*}{d\theta} = \frac{d\sigma_s}{d\theta} S(\mathbf{q})$ . This ‘‘effective’’ scattering cross section can be used to calculate a corrected scattering mean free path based on the collective approximation  $\ell_s^*$  (see Supplemental Material [46]) and a corrected scale parameter  $s^*$ . We note here that both  $\ell_s$  and  $\ell_s^*$  are frequency dependent parameters.

Three main transport regimes are associated with the range of scale parameter  $s$  that are accurately described by the Dorokhov-Mello-Pereyra-Kumar (DMPK) equation [49,51,52]. When the scattering is weak ( $s \ll 1$ ), a ballistic transport model can be applied and  $\langle g \rangle \approx N_{\text{mod}}$ . The second regime is the diffusive regime ( $1 \ll s \ll N_{\text{mod}}$ ), where the transverse modes are strongly coupled and the average conductance decreases with the length of the sample according to the Ohm’s law

$$\langle g \rangle = N_{\text{mod}} / (1 + s). \quad (10)$$

We note that this expression can be also calculated with  $s^*$ . The DMPK equation also provides a property related to the variance of the transmission coefficient. In the diffusive regime, the variation is small and does not depend on the scale parameters of the medium. It reads as follows:

$$\text{var}(T/\langle T \rangle) = \frac{2}{3} \langle g \rangle. \quad (11)$$

As the diffusion regime is isotropic by definition and produces small variations in the transmission coefficient from a disordered realization to another, we consider this quantity as

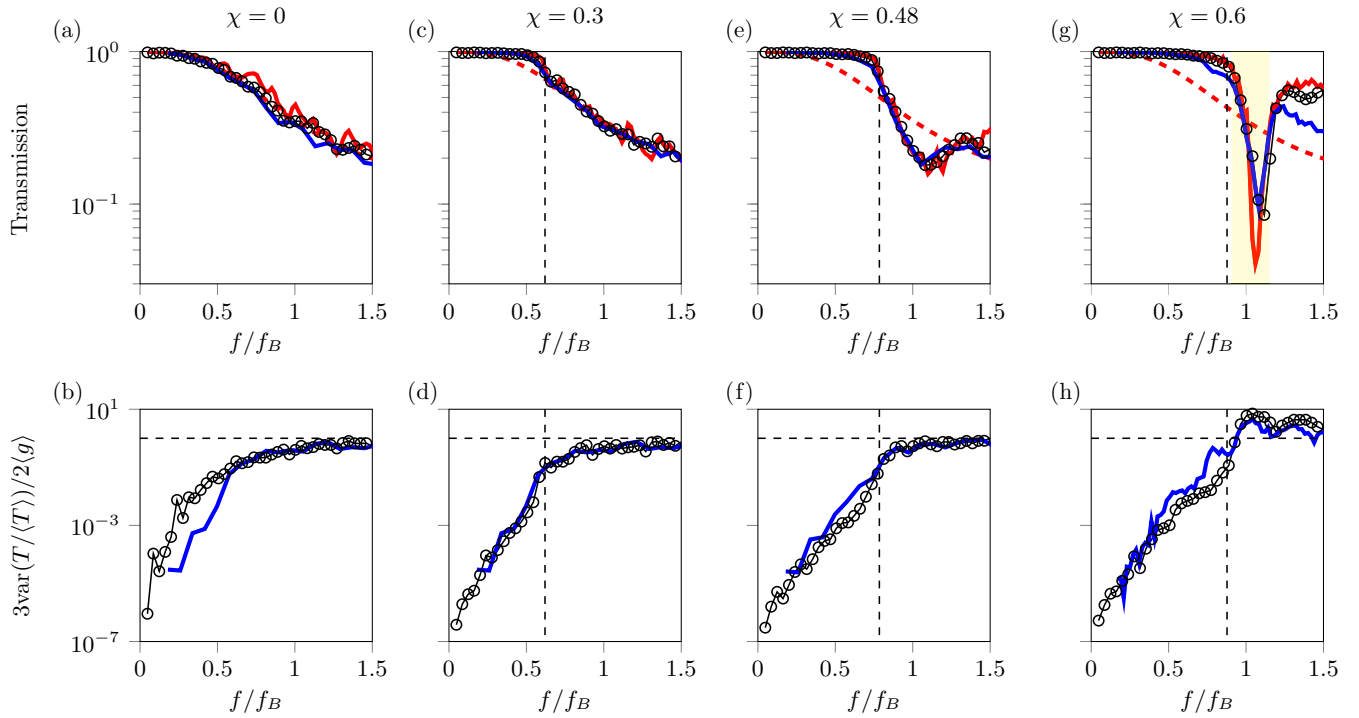


FIG. 4. [(a), (c), (e), (g)] Average transmission over 60 realizations through an hyperuniform material as a function of the frequency. The vertical dashed lines represent the cutoff frequency  $q_c$  that are determined by  $\chi$ . The red line represents the theoretical transmission deduced from the Ohm's law using the theoretical mean free path of the random media (see Supplemental Material [46]). This line is the same for all the cases, as the scatters are the same, so the scattering cross section, as well as the density of scatterers. Results using the multimodal procedure are displayed in blue lines and results using COMSOL computation are displayed by the black lines with open circles. The band gap of the perfectly crystallized media is highlighted by the yellow zone in the  $\xi = 0.6$  case (see Supplemental Material [46]). [(b), (d), (f), (h)] Variance of the transmission as a function of the frequency compared to the theoretical results  $3\text{var}(T/\langle T \rangle)/2\langle g \rangle$  [from Eq. (11)].

a threshold to measure the isotropy of the structure. Finally, when  $s \gg N_{\text{mod}}$ , the probability of a wave to return to the same coherent volume is not negligible. The interference generated in this volume traps the waves to a finite region of space. The conductance of the medium drops drastically and a transition occurs from the diffusive to the localized regimes.

When losses are accounted for in disordered material, the absorption length  $\ell_a$  must be introduced. Two regimes are distinguished depending on the value of this absorption length. The first regime appears when the losses are strong, i.e., when the absorption length is much smaller than the mean free path, i.e.,  $\ell_a \ll \ell_s$ . In this case, the wave is exponentially damped,  $T = \exp(-L_s/\ell_a)$ , before the scattering effects appear. The scattering of the wave is negligible and the effect of hyperuniformity and other phenomena arising from scattering are not observed. The second regime appears when the losses are weak, i.e., when the absorption length is much larger than the mean free path, i.e.,  $\ell_a \gg \ell_s$ . The wave scattering coexists with the losses and an absorbing diffusive transport of the wave takes place.

The generalized DMPK equation for disordered systems has been widely studied by Brouwer [53] in the absorbing diffusive regime and the transmission can be derived as

$$g_B(s, s_a) = \frac{N_{\text{mod}}}{s_a \sinh\left(\frac{s}{s_a}\right) + 1}, \quad (12)$$

where  $s_a \equiv \xi_a/\ell_s$ , with  $\xi_a = \sqrt{\ell_a \ell_s}/2$ , is the diffusive absorption length, in mean free path units. Notice, here, that the effects of correlation can be also considered by using  $s^*$  and  $\ell_s^*$  in Eq. (12).

### C. Numerical and theoretical results in the absence of loss

We start the discussion by comparing the transmission coefficients of different stealthy hyperuniform materials with different values of  $\chi$  ranging from uncorrelated random to periodic patterns. The transmission coefficients are calculated and compared when using the multimodal method, the finite elements numerical method as well as the Ohm's law calculated from the classical mean free path and the corrected mean free path from the collective approximation. In this section, we do not consider losses, which will be addressed in the next section.

Figure 4(a) shows the average transmission over 60 realizations with  $\chi = 0$  calculated by both the multimodal method (blue continuous line) and the full wave numerical simulations (black line with open black circles). The predictions by the Ohm's law with the classical mean free path are shown by the red dashed line while those corresponding to the collective approximation are shown by the red continuous line. For this case in which the point distribution does not have any correlation, all the methods provide the same behavior, as expected. In addition to these results, Fig. 4(b) shows  $3\text{var}(T/\langle T \rangle)/2\langle g \rangle$

in terms of frequency. This quantity tends to 1 when the frequency increases.

Figures 4(c) and 4(d) show the corresponding averaged results for 60 realizations with  $\chi = 0.3$ . Vertical line shows the limit  $2\sqrt{\chi/N}$  imposed by  $\chi$ , so the transparency region. As previously discussed, the point pattern presents a zero-structure factor for  $q_x/q_B$  smaller than this limit. As shown in Fig. 4(c), the average transmission is close to 1 in this range of frequencies, showing the characteristic transparency regime of stealthy hyperuniform materials. For frequencies higher than this limit, the transmission decreases with the frequency. The average transmission follows the Ohm's law for frequencies higher than the cutoff frequency imposed by  $\chi$ , i.e., the system behaves as a disordered media in the diffusive regime. We note that the transmission coefficient calculated with the collective approximation captures also this behavior and is close the calculated with both the multimodal and finite element methods. Figure 4(d) shows the different behaviors between the transparent and the diffusive regimes, which are in agreement with the predictions of the DMPK model, Eq. (11), in the diffusive regime.

Figures 4(e) and 4(f) show the average results over 60 realizations with  $\chi = 0.48$ . For this value, the point pattern presents a structure factor with three characteristic regions: the zero region for  $q_x < q_c$ , an isotropic region with increased values of the structure factor [see Figs. 2(g) and 2(k)], and a region of isotropic random scattering. These three behaviors can be identified for the wave transport properties shown in Fig. 4(e). For  $q_x < q_c$  the transparent region of the stealthy hyperuniform material is shown. Just after the limit  $q_x = q_c$ , the transmission presents a dip due to the isotropic region with increased structure factor. The value of the transmission is smaller than that predicted by the Ohm's law with the classical mean free path. When the collective approximation (red continuous line) is used, the Ohm's law reproduces well the transmission as calculated with both the multimodal and the finite element methods. This behavior is typical of an isotropic band gap although the point distribution is not periodic. For higher frequencies, the transmission coefficients follow again the Ohm's law, which means that the system falls back into the diffusive behavior. Figure 4(f) shows the variance, the behavior of which is in accordance with the previous discussion.

Finally, Figs. 4(g) and 4(h) show the averaged results over 60 realizations with  $\chi = 0.6$ . The point distribution is closer to a periodic pattern. In this case, we can clearly see the transparency region at low frequencies and the presence of the band gap due to the periodicity. The behavior of the system does not follow the Ohm's law calculated with the classical mean free path, meaning that the scattering is anisotropic. Instead, if the collective approximation is used, the corrected mean free path, exhibits the sharper features in frequency and angular dependence due to the oscillations of the structure factor, recovering the effects of the correlation. The yellow area represents the band gap of a triangular lattice as calculated in the Supplemental Material [46]. A transmission dip appears in the frequency range of the band gap of the regular lattice showing the hints of periodicity for the structures with  $\chi \gtrsim 0.5$ .

#### D. Experimental results: Lossy hyperuniform media

In this section, we experimentally characterize the wave transport properties of the stealthy hyperuniform materials for airborne sound. For these waves, the losses are unavoidable. They arise from different dissipation mechanisms in complex quasi-1D waveguides that occurs at the scatterer boundaries, in the background medium and at the waveguide walls. Their effects on the wave transport properties of the hyperuniform materials are analyzed. Here, we consider the same configurations as described above accounting for the thermal and viscous losses in the propagation of acoustic waves by simply adding an imaginary part to the wavenumber in the wave equation for the sake of simplicity.

Figures 5(a) and 5(b) show the image of a stealthy hyperuniform material and its transmission properties respectively for the case  $\chi = 0$ , i.e., for a random distribution of scatterers embedded in the rectangular waveguide. Continuous blue line in Fig. 5(b) shows the experimental transmission averaged over 3 realizations (the set of experimental transmissions coefficients for the three realizations are shown with the bluish lines). These results have been used to evaluate the absorption length of the system, which is  $\ell_a = 2.5$  m. Red line represents the transmission calculated by the Ohm's law using the collective approximation, Eq. (12). Black continuous line shows the numerical results, obtained from the multimodal method, averaged over 60 realizations. The grey area shows the standard deviation. We can observe that the medium presents the behavior predicted by the Ohm's law as for diffusive transport in disordered media.

Figures 5(c) and 5(d) show the image of a stealthy hyperuniform material and the corresponding average results with  $\chi = 0.3$ . As previously, vertical line shows the limit imposed by  $\chi$ , i.e.,  $q_c$ . The average transmission represented in Fig. 4(c) shows the characteristic transparency region of stealthy hyperuniform materials but with an amplitude smaller than the one calculated in the absence of loss, see Fig. 4. This represents a quasitransparent region. For frequencies higher than the limit  $q_c$ , we see that the transmission decreases with the frequency. Interestingly, while the average transmission does not follow the Ohm's law in the transparent region, the averaged transmission follows the Ohm's law for higher frequencies than  $q_c$ , i.e., the system behaves as a disordered media in the absorbing diffusive regime.

Figures 5(e) and 5(f) show the image of a stealthy hyperuniform material and the corresponding results for  $\chi = 0.48$ . For this case, the three characteristic regions can be identified even in the presence of losses in Fig. 5(f). For  $q_x < q_c$  the characteristic quasitransparent region is shown. Just after the limit  $q_x = q_c$ , a dip of transmission is shown due to the isotropic scattering with increased structure factor. This behavior is also captured by the Ohm's law calculated with the collective approximation, capturing the effect of correlation.

Finally, Figs. 5(g) and 5(h) show the image of a stealthy hyperuniform material and the corresponding results for  $\chi = 0.6$ . In this case, we can clearly see the quasi-transparency region at low frequencies and the presence of the band gap due to the hints of periodicity of the material. We can see that the transmission dip appears in this frequency range coming also from the hints of periodicity for the structures with



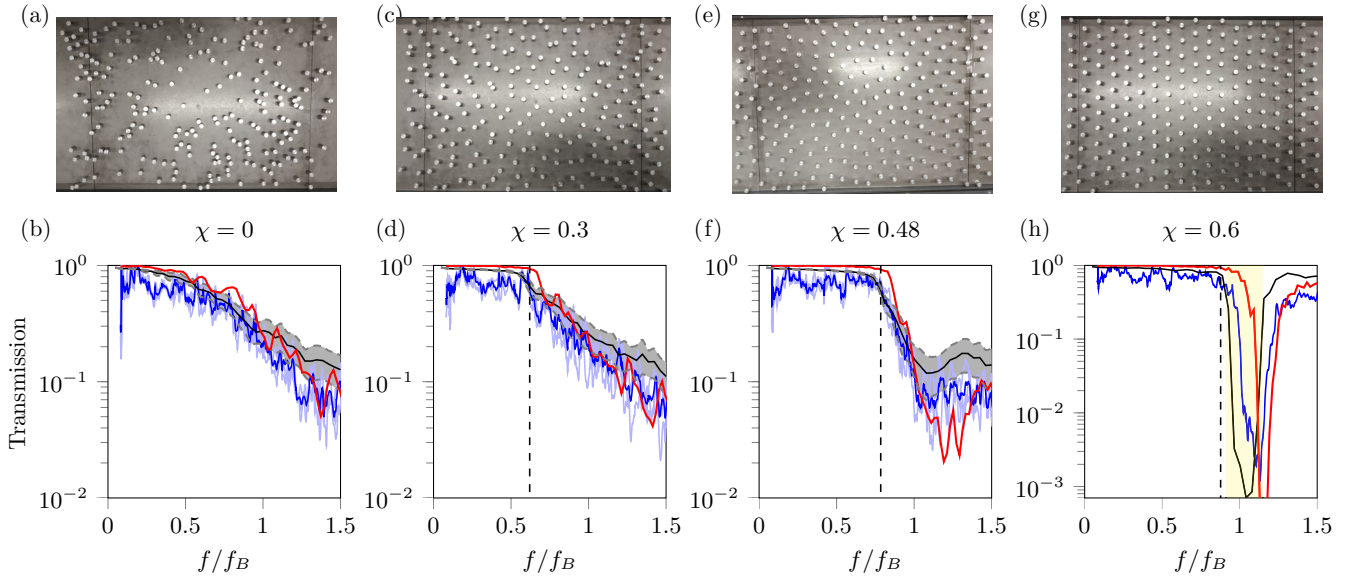


FIG. 5. [(a), (c), (e), (g)] Picture of the scatterers distributions used for the experimental study. [(b), (d), (f), (h)] Average transmission through a hyperuniform material as a function of the frequency. Blue lines display the experimental results averaged over 3 realizations. Bluish lines show the experimental transmission coefficient from all measurements. The numerical results averaged over 60 realizations are represented by the black line with a standard deviation displayed by the gray zone. Red lines show the transmission calculated by using the collective approximation together with the Eq. (12) for lossy disordered system.  $\ell_a = 2.5$  m is used as a constant absorption length. The vertical lines represents the cutoff frequency  $k_c$  determined by Eq. (2).

$\chi \gtrsim 0.5$ . In this case the dip in transmission calculated by the Ohm's law with the collective approximation falls in a different frequency because it is angularly averaged, while the experimental results are done for the normal incidence.

#### IV. CONCLUSIONS

In this paper, we have experimentally and numerically analyzed the transport properties of 2D stealthy hyperuniform materials made of rigid scatterer distributions embedded in a waveguide for acoustic waves in the audible regime. The nonresonant character of the scatterers allows linking the properties of the structure factor in the reciprocal space with the scattering properties. This shows the presence of tips of transmission by avoiding the need of local resonances. The stealthiness  $\chi$  imposes a cutoff frequency up to which the structure factor is zero, implying that materials made of rigid scatterer hyperuniform distributions are transparent to waves with frequencies lower than this cut-off frequency. These configurations have been also experimentally and numerically analyzed in order to see the feasibility of the structures for the acoustic characterization and for the analysis of the effect of

the losses and correlation in the wave transport properties. The losses have been accounted for the system via the absorption length that has been phenomenologically recovered from the experiments and used in the theoretical predictions through the generalized DMPK equation. The effect of correlation has been accounted for by the collective approximation, i.e., by correcting the scattering cross section by the structure factor. Both the effect of losses and the effect of correlation are well captured by the finite element method and by the theoretical predictions with the collective approximation in good agreement with the experiments. These results open venues to the control of acoustic waves with disordered materials with target scattering properties.

#### ACKNOWLEDGMENTS

This work has been funded by the project HYPERMETA funded under the program Étoiles Montantes of the Région Pays de la Loire and by the ANR-RGC METARoom (ANR-18-CE08-0021) project. This publication is part of the R&D&I Project/Grant No. PID2020-112759GB-I00 funded by MCIN/AEI/10.13039/501100011033/.

- [1] T. Schwartz, G. Bartal, S. Fishman, and M. Segev, *Nature (London)* **446**, 52 (2007).
- [2] D. S. Wiersma, *Nat. Photonics* **7**188 (2013).
- [3] Z. Lu, S. Shi, J. A. Murakowski, G. J. Schneider, C. A. Schuetz, and D. W. Prather, *Phys. Rev. Lett.* **96**, 173902 (2006).
- [4] C. Luo, S. G. Johnson, J. D. Joannopoulos, and J. B. Pendry, *Phys. Rev. B* **65**, 201104(R) (2002).

- [5] J. D. Joannopoulos, S. G. Johnson, J. N. Winn, and R. D. Meade, *Photonic Crystals. Molding the Flow of Light* (Princeton University Press, Princeton, 2008)
- [6] P. Deymier, ed., *Acoustic Metamaterials and Phononic Crystals* (Springer, New York, 2013).
- [7] E. Yablonovitch, *Phys. Rev. Lett.* **58**, 2059 (1987).
- [8] S. John, *Phys. Rev. Lett.* **58**, 2486 (1987).

- [9] M. Sigalas and E. Economou, *J. Sound Vib.* **158**, 377 (1992).
- [10] M. S. Kushwaha, P. Halevi, L. Dobrzynski, and B. Djafari-Rouhani, *Phys. Rev. Lett.* **71**, 2022 (1993).
- [11] E. Lidorikis, M. M. Sigalas, E. N. Economou, and C. M. Soukoulis, *Phys. Rev. Lett.* **81**, 1405 (1998).
- [12] E. Lidorikis, M. M. Sigalas, E. N. Economou, and C. M. Soukoulis, *Phys. Rev. B* **61**, 13458 (2000).
- [13] G. Mie, *Ann. Phys.* **25**, 377 (1908).
- [14] C. F. Bohren and D. R. Huffman, *Absorption and Scattering of Light by Small Particles* (Wiley, New York, 1983).
- [15] C. Rockstuhl and F. Lederer, *New J. Phys.* **8**, 206 (2006).
- [16] T. Amoah, Designer Disordered Complex Media: Hyperuniform Photonic and Phononic Band Gap Materials, Ph.D. thesis, University of Surrey, 2016.
- [17] W. Man, M. Florescu, E. P. Williamson, Y. He, S. Rez, Hashemizad, B. Y. C. Leung, D. R. Liner, S. Torquato, P. M. Chaikin, and P. J. Steinhardt, *Proc. Natl. Acad. Sci. USA* **110**, 15886 (2013).
- [18] W. Man, M. Florescu, K. Matsuyama, P. Yadak, G. Nahal, S. Hashemizad, E. Williamson, P. Steinhardt, S. Torquato, and P. Chaikin, *Opt. Express* **21**, 19972 (2013).
- [19] O. Leseur, R. Pierrat, and R. Carminati, *Optica* **3**, 763 (2016).
- [20] G. Gkantzounis, T. Amoah, and M. Florescu, *Phys. Rev. B* **95**, 094120 (2017).
- [21] G. J. Aubry, L. S. Froufe-Pérez, U. Kuhl, O. Legrand, F. Scheffold, and F. Mortessagne, *Phys. Rev. Lett.* **125**, 127402 (2020).
- [22] A. Rohfritsch, J.-M. Conoir, T. Valier-Brasier, and R. Marchiano, *Phys. Rev. E* **102**, 053001 (2020).
- [23] V. Romero-García, É. Chéron, S. Kuznetsova, J.-P. Groby, S. Félix, V. Pagneux, and L. M. Garcia-Raffi, *APL Mater.* **9**, 101101 (2021).
- [24] S. Torquato and F. H. Stillinger, *Phys. Rev. E* **68**, 069901 (2003).
- [25] O. U. Uche, F. H. Stillinger, and S. Torquato, *Phys. Rev. E* **70**, 046122 (2004).
- [26] R. D. Batten, F. H. Stillinger, and S. Torquato, *J. Appl. Phys.* **104**, 033504 (2008).
- [27] S. Torquato, G. Zhang, and F. H. Stillinger, *Phys. Rev. X* **5**, 021020 (2015).
- [28] S. Torquato, *Phys. Rev. E* **94**, 022122 (2016).
- [29] L. S. Froufe-Pérez, M. Engel, P. F. Damasceno, N. Muller, J. Haberkro, S. C. Glotzer, and F. Scheffold, *Phys. Rev. Lett.* **117**, 053902 (2016).
- [30] Y. Fan, J. K. Percus, D. K. Stillinger, and F. H. Stillinger, *Phys. Rev. A* **44**, 2394 (1991).
- [31] S. Torquato and J. Kim, *Phys. Rev. X* **11**, 021002 (2021).
- [32] J. Kim and S. Torquato, *New J. Phys.* **22**, 123050 (2020).
- [33] L. S. Froufe-Pérez, M. Engel, J. J. Sáenz, and F. Scheffold, *Proc. Natl. Acad. Sci. USA* **114**, 9570 (2017).
- [34] M. Bruneau, *Fundamentals of Acoustics* (ISTE Ltd., London, 2006).
- [35] G. M. Conley, M. Burrelli, F. Pratesi, K. Vynck, and D. S. Wiersma, *Phys. Rev. Lett.* **112**, 143901 (2014).
- [36] G. Zhang, F. H. Stillinger, and S. Torquato, *Phys. Rev. E* **92**, 022119 (2015).
- [37] G. Zhang, F. H. Stillinger, and S. Torquato, *Phys. Rev. E* **92**, 022120 (2015).
- [38] C. Kittel, *Introduction to Solid State Physics*, 8th edition (Wiley, Hoboken, NJ, 2004).
- [39] N. W. Ashcroft and N. D. Mermin, *Solid State Physics* (Holt, Rinehart, and Winston, Orlando, FL, 1976).
- [40] A. Mosk, A. Lagendijk, G. Leroosey, and M. Fin, *Nat. Photonics* **6**, 283 (2012).
- [41] V. Pagneux, *J. Comput. Appl. Math.* **234**, 1834 (2010).
- [42] A. Maurel and J.-F. Mercier, *J. Acoust. Soc. Am.* **131**, 1874 (2012).
- [43] A. Maurel, J.-F. Mercier, and S. Félix, *J. Acoust. Soc. Am.* **135**, 165 (2014).
- [44] A. Maurel, J.-F. Mercier, and S. Félix, *J. Opt. Soc. Am. A* **32**, 979 (2015).
- [45] S. Félix and V. Pagneux, *J. Acoust. Soc. Am.* **110**, 1329 (2001).
- [46] See Supplemental Material at <http://link.aps.org/supplemental/10.1103/PhysRevB.106.064206> for more details on the calculations.
- [47] V. Pagneux and A. Maurel, *J. Acoust. Soc. Am.* **116**, 1913 (2004).
- [48] Y. Imry and R. Landauer, *Rev. Mod. Phys.* **71**, S306 (1999).
- [49] O. Dorokhov, *Solid State Commun.* **51**, 381 (1984).
- [50] P. Mello, P. Pereyra, and N. Kumar, *Ann. Phys.* **181**, 290 (1988).
- [51] Y. Imry, *Europhys. Lett.* **1**, 249 (1986).
- [52] J. B. Pendry, A. MacKinnon, and P. J. Roberts, *Proc. R. Soc. A* **437**, 67 (1992).
- [53] P. W. Brouwer, *Phys. Rev. B* **57**, 10526 (1998).